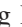




Centrifugal-Force-Induced Flow Bifurcations in Turbulent Thermal Convection


Yun-Bing Hu (胡云炳)^{1,2} Shi-Di Huang (黄仕迪)^{1,2,3} Yi-Chao Xie (谢毅超)^{4,2} and Ke-Qing Xia (夏克青)^{1,2,3,*}

¹Center for Complex Flows and Soft Matter Research and Department of Mechanics and Aerospace Engineering, Southern University of Science and Technology, Shenzhen 518055, China

²Department of Physics, The Chinese University of Hong Kong, Shatin, Hong Kong, China

³Guangdong Provincial Key Laboratory of Turbulence Research and Applications, Department of Mechanics and Aerospace Engineering, Southern University of Science and Technology, Shenzhen 518055, China

⁴State Key Laboratory for Strength and Vibration of Mechanical Structures and School of Aerospace, Xi'an Jiaotong University, Xi'an 710049, China

 (Received 20 February 2021; revised 1 August 2021; accepted 8 November 2021; published 9 December 2021)

An important and unresolved issue in rotating thermal turbulence is when the flow starts to feel the centrifugal effect. This onset problem is studied here by a novel experiment in which the centrifugal force can be varied over a wide range at fixed Rossby numbers by offsetting the apparatus from the rotation axis. Our experiment clearly shows that the centrifugal force starts to separate the hot and cold fluids at the onset Froude number 0.04. Additionally, this flow bifurcation leads to an unexpected heat transport enhancement and the existence of an optimal state. Based on the dynamical balance and characteristics of local flow structures, both the onset and optimal states are quantitatively explained.

DOI: 10.1103/PhysRevLett.127.244501

Rotationally influenced convective flows are ubiquitous in nature and in many engineering applications, particularly in geophysical and astrophysical systems (e.g., [1,2]). Many efforts were devoted to the geostrophic regime of rotating thermal turbulence, which is believed to be relevant to the flows in these systems (e.g., [3–6]). A much less studied regime is the one with non-negligible centrifugal effects. This regime can be very important in some astrophysical systems such as Jupiter, the Froude number Fr (the ratio of the centrifugal force over gravity g) of which is 2 orders of magnitude larger than that on Earth [1]. In fact, when the centrifugal effects will set in remains unsettled. Previous studies on this issue mainly focused on the properties near the onset of convection [7–12] and only recently has the role of centrifugal effects in turbulent convection received some attention [13,14].

In this Letter, we present a novel experiment aimed at studying the onset of centrifugal effects in turbulent rotating Rayleigh-Bénard convection (RRBC), where a rotating fluid layer is heated from below and cooled from above. Unlike the conventional axisymmetric RRBC, the convection cell in the present study was placed at a distance $d = de_d$ away from the rotation axis [see the inset of Fig. 1(a)]. This innovative setup can not only generate a large centrifugal force with a smaller flow domain and/or a lower rotation rate but also allows one to vary the Fr number under a fixed Rossby number Ro (the ratio of the buoyancy over the Coriolis force). With these advantages, which are almost impossible to achieve in conventional laboratory settings, we provide clear evidence that the

centrifugal force begins to separate the hot and cold fluids at $Fr \simeq 0.04$. This flow bifurcation leads to the condensation of coherent structures and consequently a remarkable heat-transport enhancement in contrast to the intuition that centrifugal dynamics would inhibit the vertical transport. Based on the balance of local flow dynamics, we quantitatively explain why the centrifugal effect occurs at $Fr \simeq 0.04$. We also provide an understanding on the universal heat-transport behavior with respect to the centrifugal buoyancy in terms of the properties of the coherent structures.

The convection cell used in the experiment consists of a cylindrical sidewall, a bottom plate where the heat flux q was applied and a top plate cooled by a temperature-controlled circulator [18]. Its radius and height are $R = 97.1$ mm and $H = 194.2$ mm, respectively, and thus the aspect ratio $\Gamma = 2R/H$ is unity. In the offset configuration, the centrifugal buoyancy force felt by a fluid parcel with temperature T can be written as $F_c = -\alpha(T - T_0)\Omega^2(\mathbf{r}_\perp + \mathbf{d})$ [see the inset of Fig. 1(a)]. Here, \mathbf{r}_\perp is the parcel's perpendicular distance from the cell's central axis, Ω is the rotation rate, and T_0 is a reference temperature. We nondimensionalize F_c by the gravitational buoyancy force $\alpha g \Delta T$, yielding $F'_c = -(Fr_R \mathbf{r}'_\perp + Fr_d \mathbf{e}_d)T'$, where $\mathbf{r}'_\perp = \mathbf{r}_\perp/R$ and $T' = (T - T_0)/\Delta T$ with ΔT ($= 16.0$ K) being the temperature difference over the fluid layer. Here, $Fr_R = \Omega^2 R/g$ is the usual Fr number that characterizes the axisymmetric centrifugal force along the cell's radial direction, and $Fr_d = \Omega^2 d/g$ describes the new “directed” centrifugal force along \mathbf{d} . The ratio of these two numbers

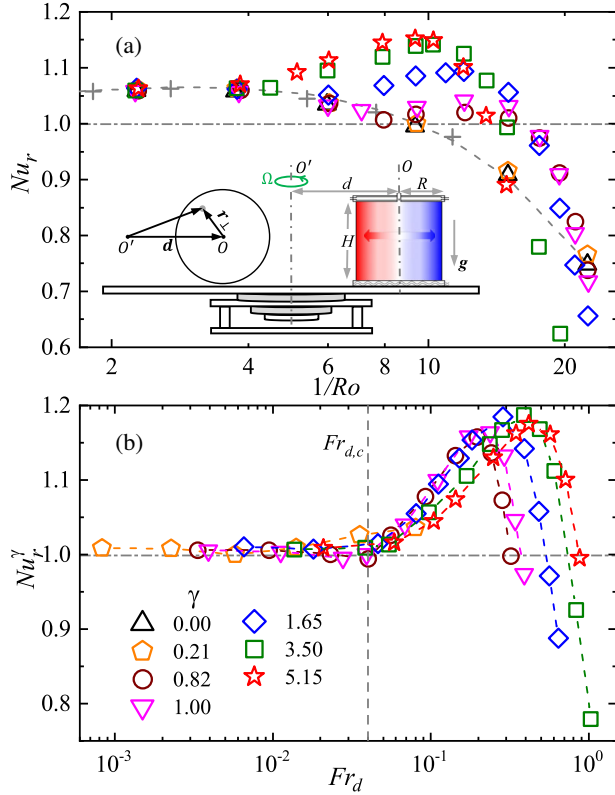


FIG. 1. (a) The reduced Nu number Nu_r as a function of $1/Ro$ for different γ . Gray dashed line: a (log + linear) fitting [15] to the data with $\gamma = 0$. Gray plus: data taken from [16] with the Ra effects eliminated [17]. (b) Another reduced Nu number Nu_r^γ as a function of Fr_d . The vertical dashed line indicates the sharp onset at $Fr_{d,c} \approx 0.04$. Inset in (a): A sketch of the experimental setup. The solid circle on the left is a top view of the convection cell, showing how the centrifugal force felt by a fluid parcel at position $\mathbf{d} + \mathbf{r}_\perp$ can be decomposed into an axisymmetric part $\Omega^2 \mathbf{r}_\perp$ and a directed one $\Omega^2 \mathbf{d}$.

equals the dimensionless offset distance $\gamma = d/R$, which varied from 0 to 5.15 in the experiment. The Rayleigh number $Ra = \alpha g \Delta T H^3 / (\nu \kappa)$ was fixed at 4.4×10^9 and the Prandtl number $Pr = \nu / \kappa$ at 4.34. The rotation rate Ω changed from 6 to 60 rpm, resulting in the convective Rossby number $Ro = (\alpha g \Delta T / H)^{1/2} / (2\Omega)$ varying from 0.045 to 0.44. We measured the heat transfer efficiency (Nusselt number $Nu = qH/k\Delta T$) and the flow fields with particle image velocimetry (PIV) [18–20]. In addition, eight thermistors, equally distributed azimuthally at mid-height, were inserted into the sidewall to detect the flow dynamics [26,27]. The properties of the working fluid water, i.e., the thermal expansion coefficient α , the kinematic viscosity ν , the thermal diffusivity κ , and the thermal conductivity k , were calculated at $T_0 = 40.0^\circ\text{C}$.

Figure 1(a) shows the reduced Nu number $Nu_r = Nu/Nu(1/Ro = 0)$ versus $1/Ro$, which has been used to examine the Coriolis effects in RRBC [16,28]. Our data with $\gamma = 0$ is seen to agree well with those from previous

studies [16] and can be well fitted by a (log + linear) function [15]. But for the offset cases with $\gamma \geq 0.82$, Nu_r increases remarkably from the reference data when $1/Ro$ ($\propto \Omega$) exceeds a critical value. This unexpected heat-transport enhancement indicates that there must exist some new effects for the offset system. Close examination reveals that the enhancement occurs at different critical rotation rates for different γ , implying the importance of $Fr_d (\propto \Omega^2 d)$.

To focus on the effects of Fr_d , we define another reduced Nu number $Nu_r^\gamma = Nu/Nu(\gamma = 0)$ [29]. Figure 1(b) shows that when Nu_r^γ is plotted against Fr_d , all data sets collapse at small Fr_d but then increase significantly when Fr_d is larger than an onset value $Fr_{d,c} \approx 0.04$ and drops sharply after reaching a maximum value $Nu_{r,\max}^\gamma$ at $Fr_{d,\max}$ [20]. This result shows clearly that the heat-transport enhancement relative to the $\gamma = 0$ case is due to the centrifugal force. As it is generally thought that centrifugal effects primarily lead to a reduction in heat transfer [7,11,12], this counterintuitive enhancement needs a physical understanding.

Figure 2 shows how the centrifugal force modifies the flow structure, which can influence the global transport in varying degrees [19,26,30–32]. For the $\gamma = 0$ cases, one sees that the magnitude of the vertical velocity decreases significantly with increasing $1/Ro$; meanwhile, the columnar structures become more vertically uniform and horizontally confined, which can be understood via the Taylor-Proudman effect. For the offset case with $Fr_d < Fr_{d,c} \approx 0.04$ [Fig. 2(b)], one sees no appreciable difference from the $\gamma = 0$ case with the same rotation rate [Fig. 2(a)]. However, when $Fr_d > 0.04$ [Figs. 2(d) and 2(f)], instead of being greatly suppressed by rotation, the maximum vertical velocity is increased manyfold. Another important feature for the large Fr_d cases is that the cold downwelling (hot upwelling) flows are now concentrated near the right (left) region. As a result, the central bulk flow becomes much “quieter.” If we calculate the percentages of the kinetic energy contained in the 30% area of the whole field near the sidewall (15% for each side), the figures are 37% and 57% for the cases of Figs. 2(e) and 2(f), respectively [20]. This happens because the cold and hot fluids will be separated and move away from or close to the rotation axis when the centrifugal force sets in. The sidewall will stop their horizontal movements and lead these coherent structures to be condensed near the sidewall. This is a case of extreme condensation of coherent structures [33,34].

The PIV results clearly demonstrate that after the onset of centrifugal force, the flow structure bifurcates from randomly distributed columns to a state with the hot and cold fluids being separated. As it is impractical to make PIV measurements for all cases, we probe the flow structure indirectly based on the azimuthal temperature profiles at the sidewall [26,27]. Figure 3(a) shows some examples with $\gamma = 3.50$. It can be seen that all the profiles for

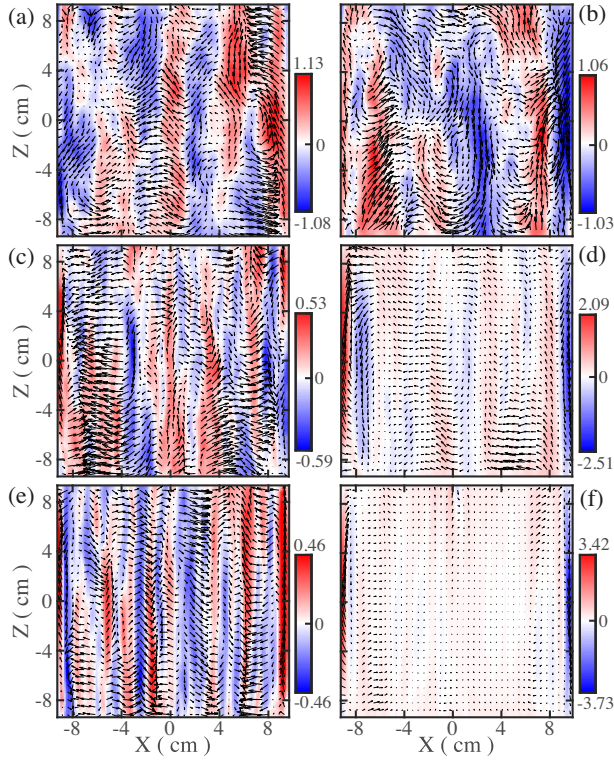


FIG. 2. Time-averaged velocity fields measured by PIV at the vertical plane passing through the rotation axis and the center line of the cell. Left panel: $\gamma = 0$; right panel: $\gamma = 3.50$. The parameter values of $[1/Ro, Fr_d]$ are (a) $[2.28, 0]$, (b) $[2.28, 0.01]$, (c) $[7.62, 0]$, (d) $[7.57, 0.15]$, (e) $[15.19, 0]$, and (f) $[15.11, 0.61]$. The color bars are coded by the vertical velocity in unit of cm/s with the maximum and minimum values indicated in the respective maps.

$1/Ro \geq 5.99$ (i.e., large rotation rates) have a sinusoidal shape [21–25,35], which is consistent with the separation of hot and cold flows seen from the PIV results. Moreover, the temperature contrast between the hot and cold fluids increases with the increased rotation rate, indicating that the separation and condensation of coherent structures become much stronger. The same behavior can be observed with the rotation rate fixed but increasing the offset distance γ [Fig. 3(b)].

To quantify how the separation behavior changes with the centrifugal force, we make a Fourier analysis of the sidewall temperature signals. Figure 3(c) shows the normalized energy of the first Fourier mode E_1/E_{total} as a function of Fr_d . The excellent collapse of all the data onto a single curve confirms that the separation behavior is indeed controlled by Fr_d . Furthermore, this curve can be well described by an empirical function $E_1/E_{\text{total}} = A \tanh[B(Fr_d - C)] + D$ [36] (green solid line), from which one can obtain two transitional Fr_d values, i.e., $(C - 1/B) = 0.012$ (vertical dashed line) and $(C + 1/B) = 0.05$ (vertical solid line). For $Fr_d < 0.012$, the lower plateau of E_1/E_{total} reflects that there is no separation of hot and cold

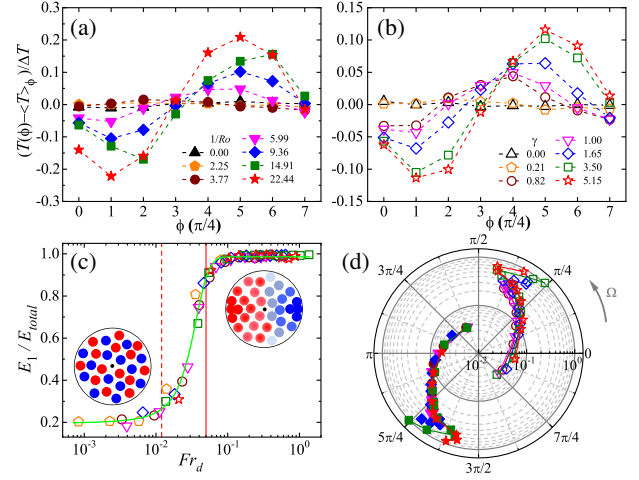


FIG. 3. The azimuthal temperature profiles with (a) fixed $\gamma = 3.50$ and (b) fixed $1/Ro = 9.36$. Here, $T(\phi)$ is the time-averaged temperature at azimuthal position ϕ (in units of $\pi/4$) and $\langle T \rangle_\phi$ is the azimuthal mean. The position of $\phi = 0$ corresponds to the point farthest to the rotation axis. (c) The normalized energy of the first Fourier mode E_1/E_{total} as a function of Fr_d , where $E_{\text{total}} = \sum_{i=1}^4 E_i$ (see text for explanation of the fitting line (green) and the two vertical lines). The two cartoons indicate the changes of the distribution of the hot and cold columns. (d) The azimuthal positions of the hottest (solid symbol) and coldest (open symbol) fluids in a polar plot with Fr_d being the radial coordinate. The gray arrow indicates the direction of rotation. (b), (c), and (d) share the same symbols.

columns and they are uniformly distributed. However, once $Fr_d > 0.012$, the flow state begins to bifurcate sharply and E_1/E_{total} takes up almost all the spectral energy at $Fr_d = 0.05$, corresponding to the extreme condensation of coherent structures near the sidewall. These two cases are illustrated by the cartoons in Fig. 3(c). Note that $Fr_d = 0.05$ is very close to the onset value $Fr_{d,c} \simeq 0.04$ obtained from the Nu_l^* data, implying that the heat-transport enhancement originates from the centrifugal force–induced bifurcation of the flow states.

We now explain why the centrifugal effect sets in at $Fr_{d,c}$. When the transition to centrifugally dominant flow occurs, the free-fall timescale of gravitational buoyancy $\tau_{\text{ff}} = \sqrt{H/\alpha g \Delta T}$ should be balanced by the centrifugal one $\tau_{\text{cb}} = \sqrt{l_0/\alpha(\Omega^2 d)\Delta T}$ [13]. Here, the typical centrifugal force is $\Omega^2 d$ due to the offset distance d and l_0 is a characteristic length scale. The dynamical balance $\tau_{\text{ff}} \simeq \tau_{\text{cb}}$ immediately leads to the onset Fr number as $Fr_{d,c} \simeq l_0/H$. Under rapid rotation, the prominent flow structures are vertically aligned columns with diffusive horizontal motions [37,38]. Only within the “mean free distance” l_0 , does the column’s horizontal motion have free-fall features. According to a previous study [38], l_0 roughly equals the column’s diameter; furthermore, for a comparable Ra as in the present study, it is found that the column’s diameter ranges from $0.03H$ to $0.05H$ [39]. Therefore,

$Fr_{d,c}$ lies in the range of $0.03 \sim 0.05$, which is in excellent agreement with the measured value 0.04 . It is noteworthy that the onset value $Fr_{d,c} \simeq 0.04$ is consistent with the widely adopted putative value of 0.05 in turbulent RRBC (e.g., [16,28]), which was first obtained for the onset of convection [10]. On the other hand, the present results differ from a recent prediction that the onset Fr number equals to $\Gamma/2$, which was obtained from “global” force balance [13,14].

The local nature of the force balance for the centrifugal effect provides us a basis to relate the present onset result to conventional RRBC. Imagine an infinitely large axisymmetric convection cell, and our cell is just like an observation window that moves along the radial direction to detect when the local centrifugal force $\Omega^2 d$ starts to separate the hot and cold fluids. This picture is supported by a recent study of conventional RRBC, which shows that the centrifugal force doesn’t manifest itself until the observed radial position is large enough [37]. Thus, the present experiment is a valid model to address the *onset* of centrifugal effect in conventional RRBC.

Although the onset of the centrifugal force is independent of the present laboratory arrangement, the flow properties after onset are not, which is clearly manifested by the spread Nu_r' for $Fr_d > 0.04$ [Fig. 1(b)]. However, their similar shape suggests that they could be governed by a generic mechanism. The PIV results reveal that as Fr_d increases, the coherency (i.e., the vortex density and the temperature contrast) of the condensed structures increases but their size decreases. The increased coherency leads to an increased velocity due to the enhanced buoyancy flux, which helps heat transport, whereas the decreased size would reduce heat transport [20]. Therefore, the competition between these two effects could be responsible for these similar Nu_r' curves.

To quantify these two competing effects, we applied the temperature extrema–extraction method [40,41] to analyze the sidewall temperature signals. Briefly, a quadratic function $T = a_2\phi^2 + a_1\phi + a_0$ is used to fit the highest (lowest) temperature signal and its two neighbors, from which the hottest ($i = h$) and coldest ($i = c$) temperatures $T_i = (4a_2a_0 - a_1^2)/4a_2$ and their spatial spreads along the azimuthal direction $\beta_i = 1/|a_2|$ can be obtained. The normalized temperature contrast $|T_i - T_{\text{bulk}}|/\Delta T$ and the normalized azimuthal spread $\beta_i/2\pi$ can be used, respectively, as a measure of the coherency and the size of coherent structures [20]. As these quantities are statistically the same for hot and cold structures, we take their average, i.e., $\delta = (T_h - T_c)/(2\Delta T)$ and $\beta = (\beta_h + \beta_c)/(4\pi)$.

Figure 4(a) shows that with increasing Fr_d , indeed the coherency δ increases and the size β decreases. At the position $Fr_{d,\max}^{\text{est}}$ where these two competing effects are comparable, an optimal state for heat transfer would be expected. The results of $Fr_{d,\max}^{\text{est}}$ for different γ are shown in Fig. 4(b) [20] and compared with $Fr_{d,\max}$ obtained from

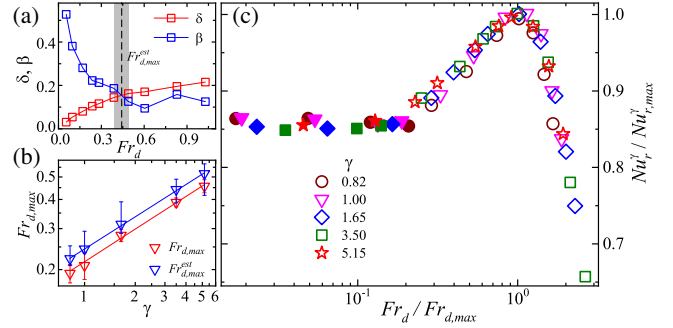


FIG. 4. (a) An example of the temperature contrast δ and azimuthal spread β as a function of Fr_d for $\gamma = 3.50$. The vertical dashed line indicates the estimated $Fr_{d,\max}^{\text{est}}$ at which these two quantities are comparable. The shaded area implies the possible values of $Fr_{d,\max}^{\text{est}}$, which is used to estimate its error bar. (b) The $Fr_{d,\max}^{\text{est}}$ from (a) are compared with $Fr_{d,\max}$ obtained from Nu_r' . The solid lines are power law fittings: $Fr_{d,\max}^{\text{est}} = 0.25\gamma^{0.46}$ and $Fr_{d,\max} = 0.22\gamma^{0.47}$. (c) The rescaled $Nu_r'/Nu_{r,\max}'$ versus $Fr_d/Fr_{d,\max}$. For clarity, solid symbols are used to label the data before onset.

Nu_r' . It can be seen that both their values and scaling exponents are very close to each other, suggesting that the present understanding and estimation have captured the underlying physics. Indeed, when the data in Fig. 1(b) are rescaled with the critical values at optimal state, they fall onto a single curve [the open symbol in Fig. 4(c)]. For strongly nonlinear systems like RRBC, the data collapse and their universal shape are remarkable, further confirming that these similar heat-transport behaviors are determined by the competition between the increased coherency and decreased size of coherent structures.

Finally, we examine how the coherent structures distribute along the sidewall after onset. Figure 3(d) shows the hottest (coldest) azimuthal positions in polar plot with Fr_d being the radial coordinate. As the hot and cold structures behave similarly, we focus on the cold ones. We first note that in RRBC without centrifugal effect a cyclonic flow will be generated near the sidewall to balance the anticyclonic flow in the bulk region [27,42–44]. This cyclonic flow would carry the cold structures to move azimuthally. However, with the presence of centrifugal force, the cold structures will be locked at a preferred azimuthal position. At small rotation rates, the cyclonic flow is not well developed [42], and the cold structures will be deflected clockwise by the Coriolis force while moving toward the sidewall, resulting in preferred positions in the range of $7\pi/4 \leq \phi \leq 0$. As the rotation rate increases, the cyclonic flow comes into play. The cold fluids will drift toward $\phi = 0$ under the joint effects of the cyclonic flow and the centrifugal force. However, these two effects become opposite for $\phi > 0$: while the cyclonic flow carries the cold fluids to move counterclockwise, the centrifugal force tends to drive them back toward $\phi = 0$. Therefore,

the azimuthal offset of these structures follows a different Fr_d -dependent trend [20]. Eventually, the fast rotation rate will suppress the cyclonic flow [27], but the centrifugal force keeps increasing, so the cold structures move back toward $\phi = 0$. We note that the separation of the hot and cold coherent structures and their shifting behaviors are quite similar to the clustering behaviors of volcanoes on Io, which are caused by the tidal force exerted by Jupiter [45–47]. Further studies are needed to ascertain whether a deeper connection exists between these two phenomena. If so, the present results may shed light on the tidal effects in astronomy.

We thank Lu Zhang for helpful discussions and Yu-Hao He for helping with the PIV measurements. This work was supported by the National Natural Science Foundation of China (NSFC) (Grant No. 12072144), the Research Grants Council of Hong Kong SAR (Grants No. N_CUHK437/15 and No. CUHK14302317), and the Department of Science and Technology of Guangdong Province (Grant No. 2019B21203001). S.-D. H. acknowledges the support from NSFC (Grants No. 11961160719 and No. 91752201). Y.-C. X. was supported in part by a NSFC grant (Grant No. 12002260), a Xi'an Jiaotong University Young Talent Support Plan, and the Fundamental Research Funds for the Central Universities.

*Corresponding author.
xiakq@sustech.edu.cn

- [1] Y. Kaspi *et al.*, Jupiter's atmospheric jet streams extend thousands of kilometres deep, *Nature (London)* **555**, 223 (2018).
- [2] J. P. Johnston, Effects of system rotation on turbulence structure: A review relevant to turbomachinery flows, *Int. J. Rotating Mach.* **4**, 582954 (1998).
- [3] E. M. King, S. Stellmach, J. Noir, U. Hansen, and J. M. Aurnou, Boundary layer control of rotating convection systems, *Nature (London)* **457**, 301 (2009).
- [4] K. Julien, E. Knobloch, A. M. Rubio, and G. M. Vasil, Heat Transport in Low-Rossby-Number Rayleigh-Bénard Convection, *Phys. Rev. Lett.* **109**, 254503 (2012).
- [5] R. E. Ecke and J. J. Niemela, Heat Transport in the Geostrophic Regime of Rotating Rayleigh-Bénard Convection, *Phys. Rev. Lett.* **113**, 114301 (2014).
- [6] R. P. J. Kunnen, The geostrophic regime of rapidly rotating turbulent convection, *J. Turbul.* **22**, 267 (2021).
- [7] J. E. Hart, On the influence of centrifugal buoyancy on rotating convection, *J. Fluid Mech.* **403**, 133 (2000).
- [8] N. Becker, J. D. Scheel, M. C. Cross, and G. Ahlers, Effect of the centrifugal force on domain chaos in Rayleigh-Bénard convection, *Phys. Rev. E* **73**, 066309 (2006).
- [9] J. M. Lopez, A. Rubio, and F. Marques, Travelling circular waves in axisymmetric rotating convection, *J. Fluid Mech.* **569**, 331 (2006).
- [10] F. Marques, I. Mercader, O. Batiste, and J. M. Lopez, Centrifugal effects in rotating convection: axisymmetric states and three-dimensional instabilities, *J. Fluid Mech.* **580**, 303 (2007).
- [11] J. M. Lopez and F. Marques, Centrifugal effects in rotating convection: nonlinear dynamics, *J. Fluid Mech.* **628**, 269 (2009).
- [12] J. Curbelo, J. M. Lopez, A. M. Mancho, and F. Marques, Confined rotating convection with large Prandtl number: Centrifugal effects on wall modes, *Phys. Rev. E* **89**, 013019 (2014).
- [13] S. Horn and J. M. Aurnou, Regimes of Coriolis-Centrifugal Convection, *Phys. Rev. Lett.* **120**, 204502 (2018).
- [14] S. Horn and J. M. Aurnou, Rotating convection with centrifugal buoyancy: Numerical predictions for laboratory experiments, *Phys. Rev. Fluids* **4**, 073501 (2019).
- [15] S. Weiss, P. Wei, and G. Ahlers, Heat-transport enhancement in rotating turbulent Rayleigh-Bénard convection, *Phys. Rev. E* **93**, 043102 (2016).
- [16] J.-Q. Zhong, R. J. A. M. Stevens, H. J. H. Clercx, R. Verzicco, D. Lohse, and G. Ahlers, Prandtl-, Rayleigh-, and Rossby-Number Dependence of Heat Transport in Turbulent Rotating Rayleigh-Bénard Convection, *Phys. Rev. Lett.* **102**, 044502 (2009).
- [17] This data set has the same control parameters as in the present experiment, except that the Rayleigh number $Ra = 2.2 \times 10^9$ is a bit smaller than the present one. So they are shifted to eliminate the Ra effects according to the scaling relations proposed in Ref. [15], i.e., $(1/Ro) \rightarrow (Ra/Ra_{\text{ref}})^{0.18}(1/Ro)$ and $Nu_r - 1 \rightarrow (Ra/Ra_{\text{ref}})^{0.35}(Nu_r - 1)$. The reference Rayleigh number here is $Ra_{\text{ref}} = 4.4 \times 10^9$.
- [18] C. Sun, K.-Q. Xia, and P. Tong, Three-dimensional flow structures and dynamics of turbulent thermal convection in a cylindrical cell, *Phys. Rev. E* **72**, 026302 (2005).
- [19] C. Sun, H.-D. Xi, and K.-Q. Xia, Azimuthal Symmetry, Flow Dynamics, and Heat Transport in Turbulent Thermal Convection in a Cylinder with an Aspect Ratio of 0.5, *Phys. Rev. Lett.* **95**, 074502 (2005).
- [20] See Supplemental Material, which includes Refs. [21–25], at <http://link.aps.org/supplemental/10.1103/PhysRevLett.127.244501> for more detailed information.
- [21] E. Brown, A. Nikolaenko, and G. Ahlers, Reorientation of the Large-Scale Circulation in Turbulent Rayleigh-Bénard Convection, *Phys. Rev. Lett.* **95**, 084503 (2005).
- [22] E. Brown and G. Ahlers, Rotations and cessations of the large-scale circulation in turbulent Rayleigh-Bénard convection, *J. Fluid Mech.* **568**, 351 (2006).
- [23] Y.-C. Xie, P. Wei, and K.-Q. Xia, Dynamics of the large-scale circulation in high-Prandtl-number turbulent thermal convection, *J. Fluid Mech.* **717**, 322 (2013).
- [24] S.-L. Lui and K.-Q. Xia, Spatial structure of the thermal boundary layer in turbulent convection, *Phys. Rev. E* **57**, 5494 (1998).
- [25] H.-D. Xi and K.-Q. Xia, Azimuthal motion, reorientation, cessation, and reversal of the large-scale circulation in turbulent thermal convection: A comparative study in aspect ratio one and one-half geometries, *Phys. Rev. E* **78**, 036326 (2008).
- [26] H.-D. Xi and K.-Q. Xia, Flow mode transitions in turbulent thermal convection, *Phys. Fluids* **20**, 055104 (2008).

- [27] M. Wedi, D. P. M. van Gils, E. Bodenschatz, and S. Weiss, Rotating turbulent thermal convection at very large Rayleigh numbers, *J. Fluid Mech.* **912**, A30 (2021).
- [28] R. J. A. M. Stevens, H. J. H. Clercx, and D. Lohse, Heat transport and flow structure in rotating rayleigh-bénard convection, *Eur. J. Mech. B* **40**, 41 (2013).
- [29] Refer to the quantity $(Nu - Nu_0)/Nu_0$ defined in [13], which is used to pick out the centrifugal effect only.
- [30] X.-D. Shang, X.-L. Qiu, P. Tong, and K.-Q. Xia, Measured Local Heat Transport in Turbulent Rayleigh-Bénard Convection, *Phys. Rev. Lett.* **90**, 074501 (2003).
- [31] S.-D. Huang, M. Kaczorowski, R. Ni, and K.-Q. Xia, Confinement-Induced Heat-Transport Enhancement in Turbulent Thermal Convection, *Phys. Rev. Lett.* **111**, 104501 (2013).
- [32] L. Zwirner, A. Tilgner, and O. Shishkina, Elliptical Instability and Multiple-Roll Flow Modes of the Large-Scale Circulation in Confined Turbulent Rayleigh-Bénard Convection, *Phys. Rev. Lett.* **125**, 054502 (2020).
- [33] K.-L. Chong, S.-D. Huang, M. Kaczorowski, and K.-Q. Xia, Condensation of Coherent Structures in Turbulent Flows, *Phys. Rev. Lett.* **115**, 264503 (2015).
- [34] K. L. Chong, Y. Yang, S.-D. Huang, J.-Q. Zhong, R. J. A. M. Stevens, R. Verzicco, D. Lohse, and K.-Q. Xia, Confined Rayleigh-Bénard, Rotating Rayleigh-Bénard, and Double Diffusive Convection: A Unifying View on Turbulent Transport Enhancement Through Coherent Structure Manipulation, *Phys. Rev. Lett.* **119**, 064501 (2017).
- [35] The sinusoidal shape of these profiles is quite similar to that measured in standard Rayleigh-Bénard convection, which inspires us to analyze these profiles by the temperature extrema-extraction method on page 4. See [20] for more details.
- [36] A similar function was used to obtain the transitional points from the temperature profiles in T. Takeshita, T. Segawa, J. A. Glazier, and M. Sano, Thermal Turbulence in Mercury, *Phys. Rev. Lett.* **76**, 1465 (1996). Here, A , B , C , and D are fitting parameters in the function.
- [37] D. Noto, Y. Tasaka, T. Yanagisawa, and Y. Murai, Horizontal diffusive motion of columnar vortices in rotating Rayleigh-Bénard convection, *J. Fluid Mech.* **871**, 401 (2019).
- [38] K.-L. Chong, J.-Q. Shi, G.-Y. Ding, S.-S. Ding, H.-Y. Lu, J.-Q. Zhong, and K.-Q. Xia, Vortices as Brownian particles in turbulent flows, *Sci. Adv.* **6**, eaaz1110 (2020).
- [39] R. P. J. Kunnen, H. J. H. Clercx, and B. J. Geurts, Vortex statistics in turbulent rotating convection, *Phys. Rev. E* **82**, 036306 (2010).
- [40] H.-D. Xi, S.-Q. Zhou, Q. Zhou, T.-S. Chan, and K.-Q. Xia, Origin of the Temperature Oscillation in Turbulent Thermal Convection, *Phys. Rev. Lett.* **102**, 044503 (2009).
- [41] Q. Zhou, H.-D. Xi, S.-Q. Zhou, C. Sun, and K.-Q. Xia, Oscillations of the large-scale circulation in turbulent Rayleigh-Bénard convection: The sloshing mode and its relationship with the torsional mode, *J. Fluid Mech.* **630**, 367 (2009).
- [42] X. Zhang, D. P. M. van Gils, S. Horn, M. Wedi, L. Zwirner, G. Ahlers, R. E. Ecke, S. Weiss, E. Bodenschatz, and O. Shishkina, Boundary Zonal Flow in Rotating Turbulent Rayleigh-Bénard Convection, *Phys. Rev. Lett.* **124**, 084505 (2020).
- [43] X. M. de Wit, A. J. A. Guzmán, M. Madonia, J. S. Cheng, H. J. H. Clercx, and R. P. J. Kunnen, Turbulent rotating convection confined in a slender cylinder: The sidewall circulation, *Phys. Rev. Fluids* **5**, 023502 (2020).
- [44] X. Zhang, R. E. Ecke, and O. Shishkina, Boundary zonal flows in rapidly rotating turbulent thermal convection, *J. Fluid Mech.* **915**, A62 (2021).
- [45] C. W. Hamilton, C. D. Beggan, S. Still, M. Beuthe, R. M. C. Lopes, D. A. Williams, J. Radebaugh, and W. Wright, Spatial distribution of volcanoes on Io: Implications for tidal heating and magma ascent, *Earth Planet. Sci. Lett.* **361**, 272 (2013).
- [46] R. H. Tyler, W. G. Henning, and C. W. Hamilton, Tidal heating in a magma ocean within Jupiter's moon Io, *Astrophys. J. Suppl. Ser.* **218**, 22 (2015).
- [47] T. Steinke, D. van Sliedregt, K. Vilella, W. van der Wal, and B. Vermeersen, Can a combination of convective and magmatic heat transport in the mantle explain Io's volcanic pattern?, *J. Geophys. Res. Planets* **125**, e2020JE006521 (2020).